Chapter 11

Thermodynamics of a one-dimensional Bose gas

The one-dimensional (1D) regime has been recently observed in trapped Bose gases[38, 39, 40], giving strong impetus to theoretical studies of such systems. This chapter describes exact predictions of spatial correlation functions and momentum densities, which have been obtained for 1D uniform Bose gases in a grand canonical ensemble by using gauge P simulations.

A part of these results have been recently published[61].

11.1 One-dimensional uniform Bose gas at finite temperature

11.1.1 Exact solutions

The interacting uniform 1D Bose gas model described by the Hamiltonian

$$\widehat{H} = \frac{\hbar^2}{2m} \int \frac{\partial \widehat{\Psi}^\dagger(x)}{\partial x} \frac{\partial \widehat{\Psi}(x)}{\partial x} \, dx + \frac{g}{2} \int \widehat{\Psi}^{\dagger 2}(x) \widehat{\Psi}^2(x) \, dx \qquad (11.1)$$

was found to be exactly solvable several decades ago, and is one of the few exactly solvable nontrivial many-body problems[90]. The solutions were found in the pioneering works of Girardeau[91, 92] at $g \to \infty$, Lieb and Liniger[86, 93] at $T = 0$,

and by Yang and Yang[87] for the grand canonical ensemble at finite temperature $T > 0$. See also [94, 95, 96] for reviews.

Explicltly, these solutions provide a numerical algorithm to calculate a density of states ρ_k and holes ρ_h. These can then be used to obtain some intensive physical quantities of the system such as density, energy density, and pressure. Recently there have been some further advances, especially in the zero temperature and strong interactions limit. These include $T = 0$ expressions for the tails of the momentum distribution and short range $\overline{g}^{(1)}(x)$[97]; $T = 0$ expressions for $\overline{g}^{(2)}(0)$, $\overline{g}^{(3)}(0, 0)$, and $\overline{g}^{(1)}(x)$[98]; and finite T values of $\overline{g}^{(2)}(0)$[99]. These last finite temperature $\overline{g}^{(2)}(0)$ solutions indicate that there is a rich variety of correlation phenomena in the $T > 0$ regime.

Still, exact results for the vast majority of observables remain hitherto inaccessible because they cannot be obtained from the density of states and holes (or perhaps, a way to obtain them has not yet been found). This includes such basic observables as spatial correlations and even momentum distributions for $T > 0$.

The Hamiltonian (11.1) is a special case of (2.1), and as such, its grand canonical thermodynamics can be simulated using the gauge P equations (5.50) in a wide range of physical regimes. This has allowed the calculation of exact spatial correlation functions and momentum distributions for this model here — see Section 11.4.

Noteworthy in this context are also the stochastic wavefunction simulations of Carusotto and Castin[65], who calculated spatial correlation functions $\overline{g}^{(2)}(x)$ and $\overline{g}^{(1)}(x)$ of a different but related model: The canonical ensemble (i.e. with set particle number, as with all stochastic wavefunction calculations) of a uniform interacting gas in a system of small spatial extent where finite size effects were important.

11.1.2 Correspondence with trapped gases

Under present day experimental conditions, the Bose gas confinement is well approximated by a harmonic trap of transverse angular frequency $\omega_\perp$ and longitudinal frequency ω_0. The correspondence between the uniform gas model, and a trapped gas experiment can be summarized in the following points:

- The atoms behave effectively as a 1D gas provided that the transverse zero point oscillations

$$l_\perp = \sqrt{\frac{\hbar}{m\omega_\perp}} \tag{11.2}$$

are much smaller than other characteristic length scales of the system such as the healing length (11.9) and the thermal de Broglie wavelength of excitations (11.8). This regime has been reached in recent experiments[38, 39, 40].

- On length scales smaller than the trap size

$$x \ll l_0 = \sqrt{\frac{\hbar}{m\omega_0}} \tag{11.3}$$

the density of the gas is slowly varying. On this and smaller scales the 1D trapped gas and uniform gas will show the same physical behavior, and so the results obtained in Section 11.4 will be directly applicable to a trapped gas while $x \ll l_0$. It is worth noting that if, instead, details of the trap are important, a gauge P simulation with the external potential V^{ext} explicitly specified can be used instead. A dynamical example of this was given in Section 10.6.

- The field interaction strength g is related to the 3D scattering length a_s by the expression (2.19), where the effective trap cross-section in the transverse direction is[100]

$$\lambda_0 = 2\pi l_\perp^2 = \frac{2\pi\hbar}{m\omega_\perp}. \tag{11.4}$$

11.1.3   Uniform gas regimes

The properties of a the finite temperature uniform 1D gas with the Hamiltonian (11.1) depend on two dimensionless parameters: The first is the **coupling parameter**[1]

$$\gamma = \frac{mg}{\hbar^2 \rho}, \tag{11.5}$$

---

[1] Not to be confused with the unrelated single-boson loss rate γ of Chapters 6 and 7. γ is used here in Chapter 11 for the quantity (11.5) as this is the standard notation in the literature.

dependent on interaction strength g and density ρ. The ideal Bose gas is reached as $\gamma \to 0$, while the Tonks-Girardeau (TG) hard sphere gas occurs in the limit $\gamma \to \infty$. In this limit the particles undergo an effective "fermionization"[91, 92, 86, 93].

The second dimensionless parameter is the **reduced temperature**

$$\widetilde{T} = \frac{T}{T_d} = \frac{mk_B T}{2\pi\hbar^2\rho^2}, \tag{11.6}$$

where T_d is the quantum degeneracy temperature. For $T < T_d$, the gas is denser than the quantum concentration $n_Q = \sqrt{mk_B T/2\pi\hbar^2}$ and the average spacing between particles $1/\rho$ is less than the thermal de Broglie wavelength (11.8).

Several characteristic length scales in the uniform gas are:

- Mean interparticle spacing

$$l_\rho = \frac{1}{\rho}. \tag{11.7}$$

- Thermal de Broglie wavelength

$$\lambda_T = \sqrt{\frac{2\pi\hbar^2}{mk_B T}} = \frac{l_\rho}{\sqrt{\widetilde{T}}}. \tag{11.8}$$

  Atoms with typical energy behave as particles on length scales $\gg \lambda_T$, as waves on $\ll \lambda_T$

- Healing length

$$\xi^{\mathrm{heal}} = \frac{\hbar}{\sqrt{2m\rho g}} = \frac{l_\rho}{\sqrt{2\gamma}}, \tag{11.9}$$

  which is the length scale of typical spatial density fluctuations.

- Degenerate phase coherence length

$$l_\phi = \frac{\rho\lambda_T^2}{2\pi} = \frac{l_\rho}{2\pi\widetilde{T}}, \tag{11.10}$$

  which applies when $\widetilde{T} \ll 1$ and $\gamma \ll 1$. When $\widetilde{T} \gg 1$, the phase coherence length is $l_\rho = \lambda_T/\sqrt{2\pi}$.

- 1D scattering length[100]

$$a_{1D} = \frac{\hbar^2}{mg} = \frac{l_\rho}{\gamma} \tag{11.11}$$

    is the characteristic distance over which the influence of a single particle is
    felt. In the fermionized large γ regime, this is the effective size of the hard
    sphere due to a single particle.

The 1D gas behaves rather differently than the 2D and 3D cases, in that, for
example, in a strong coupling regime the density is *low*. Also, a true BEC does not
form, because long range order on length scales $\gg l_\phi$ is destroyed. This follows from
the Bogoliubov k^{-2} theorem, as explained in [101, 102]. Nevertheless, at degenerate
temperatures $\widetilde{T} \lesssim 1$ and relatively weak couplings $l_\phi \ll \xi^{\text{heal}}$ and $\gamma \ll 1$, a finite-
range quasicondensate with phase coherence exists.

11.2   Simulation details

11.2.1   Overview

Integration of the gauge P stochastic differential equations (5.50) proceeds in a sim-
ilar fashion to the dynamics calculations of Chapter 10. These are based on the
master equation formulation of the grand canonical ensemble, as described in Sec-
tion 2.6. A split-step algorithm is used, as described in Section 10.1 with integration
using the semi-implicit method described in Appendix B. To exclude potential finite-
sample bias of the kind described in Appendix A, the variance of the logarithms of
quantities to be averaged for observable estimates was also tracked.

To simulate the *uniform* gas, care needed to be taken to avoid finite size effects.
This can usually be achieved for all practical purposes by choosing a lattice spacing
several times smaller than the smallest length scale of Section 11.1.3, and a number
of lattice points large enough so that the total spatial extent is several times larger
than the largest length scale. Operationally, the lattice resolution was increased in
normal and/or momentum space until no changes with lattice resolution were seen
in the observables of interest.

There are several further issues that arise only in the thermodynamics calculations and require more detailed discussion:

11.2.2 Drift Gauge

As was discussed in more detail in Section 9.2.1, the un-gauged positive P equations are not suitable for simulation because of severe moving singularities as $\mathrm{Re}\{\alpha_{\mathbf{n}}\beta_{\mathbf{n}}\}$ takes on negative values. This behavior appears in the many-mode case as well, and leads to rapid onset of spiking, as well as possible systematic errors after only a short simulation time.

The radial drift gauge (9.17) acting locally on each mode was used to remove the moving singularities in the same manner as for the single-mode system of Chapter 9. Explicitly, when adapted to the many-mode situation this gauge is

$$\mathcal{G}_{\mathbf{n}} = i\sqrt{2\hbar\chi}\left(\alpha_{\mathbf{n}}\beta_{\mathbf{n}} - |\alpha_{\mathbf{n}}\beta_{\mathbf{n}}|\right), \tag{11.12}$$

where χ is given by (2.18), as usual.

Spiking abates, and boundary term errors are not seen.

11.2.3 Importance sampling

The simulated equations (5.50) include evolution of both amplitudes $\alpha_{\mathbf{n}}$ and weight $\Omega = e^{z_0}$. Deterministic evolution of the weight is a new feature compared to dynamics and can cause sampling problems at nonzero times $\tau > 0$.

It is convenient to initialize in Fourier space. Here the variables $\widetilde{\alpha}_{\widetilde{\mathbf{n}}}(\tau)$ and $\widetilde{\alpha}'_{\widetilde{\mathbf{n}}}(\tau)$ are given by (10.2), and bold quantities indicate vectors with M elements — one per mode. For an M-mode system of length L, the standard initial distribution (5.59) becomes in Fourier space

$$P_G(\widetilde{\boldsymbol{\alpha}}, \widetilde{\boldsymbol{\alpha}}', z_0) = \delta^2(z_0)\delta^{2M}(\widetilde{\boldsymbol{\alpha}}' - \widetilde{\boldsymbol{\alpha}})\prod_{\widetilde{\mathbf{n}}}\frac{1}{\pi\widetilde{n}_0}\exp\left(\frac{-|\widetilde{\alpha}_{\widetilde{\mathbf{n}}}|^2}{\widetilde{n}_0}\right), \tag{11.13}$$

where $\widetilde{n}_0 = L^2\overline{n}_0/2\pi M$ is the mean of all $|\widetilde{\alpha}_{\widetilde{\mathbf{n}}}|^2$ at $\tau = 0$. The lattice factors arise because the number of particles per Fourier mode is $\propto \frac{L^2}{2\pi M}$. A sample is generated

by the simple procedure

$$\widetilde{\alpha}_{\widetilde{\mathbf{n}}} = \sqrt{\widetilde{n}_0}\, \eta_{\widetilde{\mathbf{n}}} = \widetilde{\alpha}_{\widetilde{\mathbf{n}}}^{(0)} \tag{11.14a}$$

$$\widetilde{\alpha}'_{\widetilde{\mathbf{n}}} = \widetilde{\alpha}_{\widetilde{\mathbf{n}}}^{(0)} \tag{11.14b}$$

$$z_0 = 0, \tag{11.14c}$$

where the $\eta_{\widetilde{\mathbf{n}}}$ are independent complex Gaussian noises of variance unity.

The problem is that this is a good sample of the $\tau = 0$ distribution, but not necessarily so at later times. This is so even for an ideal gas when two-body interactions are absent. In the simplest case of the ideal gas with no external potential $V^{\text{ext}} = 0$, the equations of motion (5.50) can be solved exactly in Fourier space, which gives

$$\widetilde{\alpha}_{\widetilde{\mathbf{n}}}(\tau) = \widetilde{\alpha}_{\widetilde{\mathbf{n}}}^{(0)} e^{h_{\widetilde{\mathbf{n}}}(\tau)\tau} \tag{11.15a}$$

$$\widetilde{\alpha}'_{\widetilde{\mathbf{n}}}(\tau) = \widetilde{\alpha}_{\widetilde{\mathbf{n}}}^{(0)} \tag{11.15b}$$

$$z_0(\tau) = \frac{L^2}{2\pi M} \sum_{\widetilde{\mathbf{n}}} \left\{ |\widetilde{\alpha}_{\widetilde{\mathbf{n}}}(\tau)|^2 - |\widetilde{\alpha}_{\widetilde{\mathbf{n}}}^{(0)}|^2 \right\}, \tag{11.15c}$$

where

$$h_{\widetilde{\mathbf{n}}}(\tau) = \mu(\tau) - \frac{\hbar^2 k_{\widetilde{\mathbf{n}}}^2}{2m} \tag{11.16}$$

is the Gibbs factor exponent.

For the ideal gas, the exact finite temperature solution consists of an independent thermal state with mean occupation $\overline{n}_{\widetilde{\mathbf{n}}}$ for each Fourier mode. An unbiased sample of this is

$$\widetilde{\alpha}_{\widetilde{\mathbf{n}}}(\tau) = L\sqrt{\frac{\overline{n}_{\widetilde{\mathbf{n}}}(\tau)}{2\pi M}}\, \eta_{\widetilde{\mathbf{n}}} \tag{11.17a}$$

$$\widetilde{\alpha}'_{\widetilde{\mathbf{n}}}(\tau) = \widetilde{\alpha}_{\widetilde{\mathbf{n}}}(\tau) \tag{11.17b}$$

$$z_0 = 0, \tag{11.17c}$$

where for the ideal Bose gas, the mode occupations obey the Bose-Einstein distribution

$$\overline{n}_{\widetilde{\mathbf{n}}}(\tau) = \overline{n}_{\widetilde{\mathbf{n}}}^{\text{BE}}(\tau) = \frac{1}{e^{-h_{\widetilde{\mathbf{n}}}(\tau)\tau} - 1}. \tag{11.18}$$

The actual simulated $\widetilde{\alpha}_{\widetilde{\mathbf{n}}}(\tau)$ in (11.15a) are not necessarily anywhere near (11.17a) with Bose-Einstein occupations (11.18), so the nonzero variable weight (11.15c) is needed to compensate for this.

This is fine in the limit of infinite samples $\mathcal{S} \to \infty$, but in practice the distribution of the weight $\Omega = e^{z_0}$ can be badly sampled once the variance in z_0 becomes too large. Since $|\widetilde{\alpha}_{\widetilde{\mathbf{n}}}^{(0)}|^2$ is a Gaussian, then z_0 also will have a similar nature and the usual limit (7.43) for exponentials of a Gaussian applies: The weights (and hence, observable estimators, which all average quantities $\propto e^{z_0}$) are well sampled only while

$$\text{var}\left[\text{Re}\left\{z_0\right\}\right] \lesssim \mathcal{O}\left(10\right). \tag{11.19}$$

A method known as **importance sampling** offers a way to alleviate this weighting problem if one is primarily interested in the gas around a particular target time τ_T (i.e. temperature $1/k_B\tau$ and chemical potential $\mu(\tau_T)$). The importance sampling approach is widely used for weighted stochastic integration, and a comprehensive discussion of this for general situations can be found in [103], Section 7.8. In the case considered here, the idea is as follows:

In the gauge P representation, the density matrix is written as

$$\widehat{\rho}_u(\tau) = \int P_G(\tau, \boldsymbol{z}, z_0)\widehat{\Lambda}(\boldsymbol{z}, z_0)\, d^{4M}\boldsymbol{z}\, d^2 z_0, \tag{11.20}$$

where $\boldsymbol{z}$ stands for all the phase-space variables $\widetilde{\boldsymbol{\alpha}}$, $\widetilde{\boldsymbol{\alpha}}'$. The simulation here uses standard drift gauges, so that the evolution of the weight z_0 is actually deterministically dependent on the evolution of the $\boldsymbol{z}$, as given in (4.43). In the initial distribution (11.13), $z_0 = 0$ is independent of $\boldsymbol{z}$. Together, these properties allow the $\boldsymbol{z}$ and z_0 evolutions to be separated. Explicitly,

$$z_0(\tau, \boldsymbol{z}) = \int_0^\tau \frac{dz_0(\tau', \boldsymbol{z}(\tau'))}{d\tau'}\, d\tau', \tag{11.21}$$

where dz_0 is given by (4.43). After defining $\widehat{\Lambda}(\boldsymbol{z}, z_0) = e^{z_0}\,\underline{\widehat{\Lambda}}(\boldsymbol{z})$, this allows us to rewrite (11.20) as

$$\widehat{\rho}_u(\tau) = \int \underline{P}_G(\tau, \boldsymbol{z})\underline{\widehat{\Lambda}}(\boldsymbol{z})\, e^{z_0(\tau, \boldsymbol{z})}\, d^{4M}\boldsymbol{z}, \tag{11.22}$$

where the underlined quantities depend only on the amplitude variables $\boldsymbol{z}$.

The multiplying factor of the operator kernel $\underline{\widehat{\Lambda}}$ in (11.22) is $\underline{P}_G e^{z_0}$, and in fact there is a whole range of possible initial distributions provided that this factor

remains the same. In particular we could start with a different initial distribution of the amplitude variables $\underline{P}_{G0}(0, \boldsymbol{z})$ provided that this is compensated for in the initial weights by

$$z_0 = \int_0^\tau \frac{dz_0(\tau', \boldsymbol{z}(\tau'))}{d\tau'} \, d\tau' + \log \underline{P}_G(0, \boldsymbol{z}) - \log \underline{P}_{G0}(0, \boldsymbol{z}). \qquad (11.23)$$

Then (and this is the crucial point), if we could choose some initial distribution $\underline{P}_{G0}$ that leads to only a small spread in z_0 at target time τ_T, then the simulation would be well sampled there. (It would also be sampled much worse at $\tau = 0$, but this doesn't bother us). This then is the sampling according to importance (i.e. according to the situation at τ_T).

For the purposes of the simulations reported in this chapter, a fairly crude yet effective importance sampling was applied: At relatively weak coupling, a very rough but useful estimate of the state is that the Fourier modes are uncoupled, and thermally distributed with mean occupations $\overline{n}_{\widetilde{\mathbf{n}}}(\tau_T)$. The equal-weight samples (11.17) correspond to the distribution

$$\underline{P}_G^{\text{est}}(\tau_T, \boldsymbol{z}) \propto \delta^{2M}(\widetilde{\boldsymbol{\alpha}}' - \widetilde{\boldsymbol{\alpha}}) \exp\left[-\frac{2\pi M}{L^2} \sum_{\widetilde{\mathbf{n}}} \frac{|\widetilde{\alpha}_{\widetilde{\mathbf{n}}}|^2}{\overline{n}_{\widetilde{\mathbf{n}}}(\tau_T)} \right] \qquad (11.24)$$

with appropriate normalization. This is not yet quite what is wanted because the desired sampling distribution $\underline{P}_{G0}$ is to be at $\tau = 0$. An estimate of the initial distribution that leads to $\underline{P}_G^{\text{est}}(\tau, \boldsymbol{z})$ can be obtained by evolving (11.24) back in time with only kinetic interactions. This is again rather rough, since deterministic interaction terms $\propto g$ have been omitted (not to mention noise), but is simple to carry out, and was found to be sufficient for the purposes of the preliminary calculations presented here. One obtains the sampling distribution

$$\underline{P}_{G0}(0, \boldsymbol{z}) \propto \delta^{2M}(\widetilde{\boldsymbol{\alpha}}' - \widetilde{\boldsymbol{\alpha}}) \exp\left[-\frac{2\pi M}{L^2} \sum_{\widetilde{\mathbf{n}}} \frac{|\widetilde{\alpha}_{\widetilde{\mathbf{n}}}|^2}{\overline{n}_{\widetilde{\mathbf{n}}}^{(0)}} \right], \qquad (11.25)$$

where

$$\overline{n}_{\widetilde{\mathbf{n}}}^{(0)} = \overline{n}_{\widetilde{\mathbf{n}}}(\tau_T) \exp\left[-\lambda_n - h_{\widetilde{\mathbf{n}}}(\tau_T)\tau_T \right]. \qquad (11.26)$$

(Note that $\lim_{\tau \to 0}[h_{\widetilde{\mathbf{n}}}(\tau)\tau] = -\lambda_n$). Using (11.23), the initial variables are then

sampled according to

$$\widetilde{\alpha}_{\widetilde{\mathbf{n}}}(0) = L\sqrt{\frac{\overline{n}_{\widetilde{\mathbf{n}}}^{(0)}}{2\pi M}}\,\eta_{\widetilde{\mathbf{n}}} \tag{11.27a}$$

$$\widetilde{\alpha}'_{\widetilde{\mathbf{n}}}(0) = \widetilde{\alpha}_{\widetilde{\mathbf{n}}}(0) \tag{11.27b}$$

$$z_0(0) = \frac{L^2}{2\pi M}\sum_{\widetilde{\mathbf{n}}}|\widetilde{\alpha}_{\widetilde{\mathbf{n}}}(0)|^2\left(\frac{1}{\sqrt{\overline{n}_{\widetilde{\mathbf{n}}}^{(0)}}} - \frac{1}{\overline{n}_0}\right). \tag{11.27c}$$

For most of the simulations of Section 11.4, the target Fourier space distribution $\overline{n}_{\widetilde{\mathbf{n}}}(\tau_T)$ was just taken to be the plain ideal gas Bose-Einstein distribution (11.18). However, once the interactions become significant, this is not satisfactory because the actual interacting gas momentum distribution is far from the Bose-Einstein form (See e.g. Figure 11.8). A better choice of $\overline{n}_{k_{\widetilde{\mathbf{n}}}}(\tau_T)$ is the density of states function ρ_k of the exact Yang & Yang solution[87]. In practice, to simplify the calculation, an estimate of ρ_k was used instead. This was obtained by making a least squares (unweighted) fit of parameters C_{est} and σ_{est} in the expression

$$\overline{n}_{\widetilde{\mathbf{n}}} = \overline{n}_0 e^{h_{\widetilde{\mathbf{n}}}(\tau_T)\tau_T + \lambda_n} + C_{\text{est}}e^{-k_{\widetilde{\mathbf{n}}}^2\tau_T/2\sigma_{\text{est}}^2} \tag{11.28}$$

to ρ_k. This form was chosen because in the tails of the distribution in Fourier space when $k_{\widetilde{\mathbf{n}}}^2\tau_T \gg 1$, $\overline{n}_{\widetilde{\mathbf{n}}}^{(0)} \approx \overline{n}_0$, and so the initial weights $z_0(0)$ in (11.27c) are not dependent on the momentum cutoff.

11.2.4   Momentum cutoff

In a dynamical simulation, one requires that all occupied momentum modes are contained within the momentum cutoff $k_d^{\text{max}} = \pi/\Delta x_d$. Strictly speaking, this cannot ever be satisfied in these thermodynamic simulations because the $T \to \infty$ ideal gas grand canonical ensemble is used as a starting condition. This has all momentum modes occupied up to infinite energy. This turns out not to be a practical problem because the precision of calculated results is limited anyway by the finite sample size $\mathcal{S}$. It is then sufficient to increase the k_d^{max} until all observable estimates calculated are invariant with k_d^{max} to the precision achievable with a given ensemble size. This was carried out.

11.2.5   Chemical potential at intermediate temperatures

As was noted in Section 9.4, if one is primarily interested in the behavior of the system at (or around) a given temperature τ_T, and chemical potential μ, then the values of μ at intermediate times $\tau < \tau_T$ can in principle be chosen at will.

In practice, some choices lead to better precision per ensemble size than others. The analysis in Section 9.4 indicated that the single-mode simulations led to the best precision when the "effective" chemical potential $\mu_e = \frac{\partial \mu \tau}{\partial \tau}$ was roughly constant during the simulation. It was assumed that a similar dependence occurs in the many-mode system, and so, accordingly a constant μ_e was chosen so that at τ_T the chemical potential becomes $\mu(\tau_T)$. Using (9.2), the constant μ_e assumption leads to

$$\mu_e = \mu(\tau_T) + \frac{\lambda_n}{\tau_T}. \tag{11.29}$$

It remains to choose the initial density $\rho_0 = M \overline{n}_0(\lambda_n)/L$ (with initial occupation $\overline{n}_0$ given by (2.33)). It was found that for target densities $\rho(\tau_T)$ a choice of initial density

$$\rho_0 = \mathcal{O}\left(\frac{\rho(\tau_T)}{10}\right) \tag{11.30}$$

gave the best precision at τ_T in most cases. Details varied depending on system parameters, although a clear tradeoff between two noise generating processes was seen:

1. When ρ_0 was too large, a lot of added randomness is introduced into z_0 at early times, and precision is lost very rapidly once $\mathrm{var}\left[\mathrm{Re}\left\{z_0\right\}\right] \gtrsim \mathcal{O}\left(10\right)$, as discussed in Section 7.4 and Appendix A. This randomness arises largely independently of gauges or noise since the spread of $\alpha_{\mathbf{n}}$ in the initial thermal state is proportional to $\sqrt{\rho_0}$, and this then leads directly to a spread in the deterministic evolution terms of dz_0.

2. When ρ_0 is too small, excessive spread in the amplitude variables arises as well (which also then feeds into the log-weight z_0).

11.2.6 Scaling of weight variance

For uniform gas calculations it was found to be desirable to use the smallest system size that does not introduce finite size effects. The reason is that (apart from gauge-dependent terms), the weight $\Omega(\tau) = \exp \int_0^\tau \frac{dz_0}{d\tau'} d\tau'$ has the form of a Gibbs factor $\exp((\mu \overline{N} - E)/k_B T)$. This can be verified by inspection of the equations (5.50). The magnitude but also the *spread* in log-weights z_0 will thus grow with energy E and particle number $\overline{N}$. Since $\text{var}[\text{Re}\{z_0\}]$ must be $\lesssim \mathcal{O}(10)$ for good sampling of the distribution, this sets an upper limit on how large a system can be simulated.

11.3 Physical regimes simulated

11.3.1 Parameter targeting

The procedure to calculate properties at given target gas parameters γ and $\widetilde{T}$ was as follows:

1. Three physical quantities specify units. For example, m, $\hbar$, and $k_B T = 1/\tau_T$ can be chosen unity. For the purposes of investigating gases at a given γ and $\widetilde{T}$, these can be chosen arbitrarily and properties of the whole family of physical gases with those γ and $\widetilde{T}$ follow by scaling.

2. The target time τ_T is determined by the choice of units above, and the remaining essential parameters required to simulate (5.50) are g and $\mu(\tau_T)$. The coupling strength is determined by

$$g = \hbar \gamma \sqrt{\frac{k_B T}{2\pi m \widetilde{T}}},\tag{11.31}$$

   while the required target density is

$$\rho(\tau_T) = \sqrt{\frac{m k_B T}{2\pi \hbar^2 \widetilde{T}}}.\tag{11.32}$$

3. The target density is not a direct input parameter into the simulation, but it is has a one-to-one correspondence with $\mu(\tau_T)$ (while in dimensionless units).

The Yang & Yang exact solutions[87] provide an algorithm to calculate $\rho(T, \mu, g)$, and the chemical potential needed to obtain the desired density (11.32) was calculated by numerically inverting this relation.

11.3.2   Regimes attained

A wide range of physical regimes were simulated directly with the procedure described in the previous sections. In terms of the two characteristic dimensionless gas parameters γ and $\widetilde{T}$, the physical regions that have been explored are shown in Figure 11.1.

In terms of the physical regimes classification of Kheruntsyan *et al*[99] based on $\overline{g}^{(2)}(0)$ behavior (These are described in more detail in Section 11.4.1), the accessible regions are both the **quantum degenerate decoherent** and **classical decoherent** regimes, as well as the **nondegenerate fermionized** (strong coupling) regime. Simulations also access **transition regions** between these. The interesting transition region $\gamma \approx \widetilde{T} \approx \mathcal{O}(1)$ where several length scales are of the same order is also accessible in part. The lower limit of accessible $\widetilde{T}$ does not appear to be a hard limit, and more sophisticated importance sampling techniques and/or choices of $\mu_e(\tau)$ may be able to make some further inroads into lower temperature regions.

The basic limiting factor is growth of the variance of the real and/or imaginary parts of the log-weight z_0. As explained Section 11.2.6, there is a tradeoff between the variance of z_0 and the system size (e.g. lattice length L if the density is set), but there is a limit on how small the system can be made if it is to correspond to the uniform gas model. L must be significantly larger than the longest relevant length scale. However, this limit is only applicable if an unconstrained uniform gas is required. The behavior of a gas in a finite box, torus, or trap is an easier simulation and can reach temperatures not accessible for uniform gas simulations if L can be made small enough to control the growth of var $[z_0]$. The previously mentioned calculations of by Carusotto and Castin[65] for the different but related closed system model were made in such a "low temperature with finite-size effects" regime, with $\gamma \approx \mathcal{O}(0.001) - \mathcal{O}(0.01)$, $\widetilde{T} \approx \mathcal{O}(0.001) - \mathcal{O}(0.005)$.
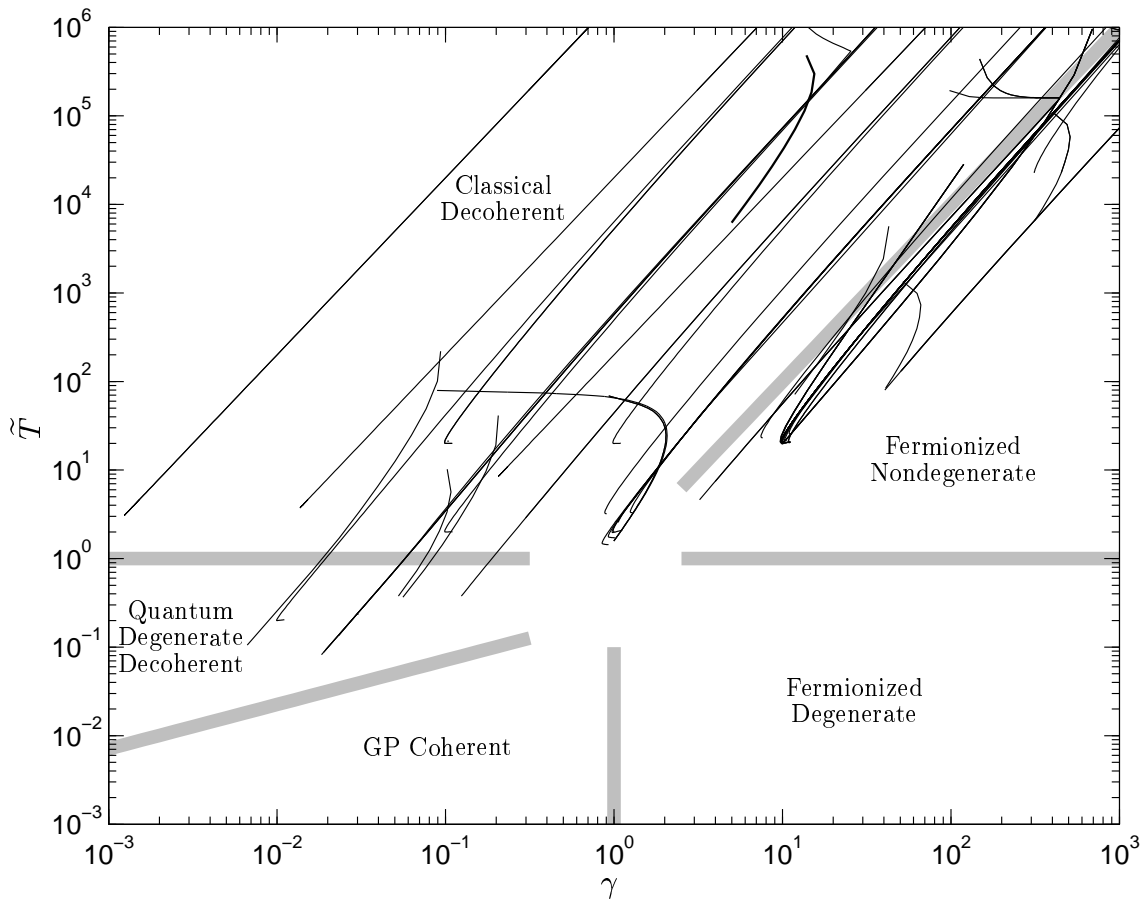
Figure 11.1: **Physical regimes attained** for the uniform interacting 1D Bose gas. DARK SOLID lines show the paths in γ, $\widetilde{T}$ parameter space taken by simulations for the τ range where useful precision in $\overline{g}^{(2)}(x)$ was obtained. Paths shown include simulations with various forms of μ_e: either given by (11.29), or by $2e^{\mu\tau} = e^{-\lambda_n} + e^{\mu(\tau_T)\tau_T} + (e^{\mu(\tau_T)\tau_T} - e^{-\lambda_n})\cos[4\pi(\tau - \tau_T)/3\tau_T]$ described in [61]. The constant form (11.29) was found to be as good or superior at reaching low temperatures. THICK SHADED bars indicate approximate transition regions between physical regimes based on the classification by Kheruntsyan *et al*[99] on the basis of $\overline{g}^{(2)}(0)$.

11.4 Observable predictions

11.4.1 Spatial correlation functions

A classification of uniform gas behaviors based on the local second order correlation function $\overline{g}^{(2)}(0)$ has been determined from the Yang & Yang solution by Kheruntsyan *et al*[99]. In this chapter, the finite temperature behavior of $\overline{g}^{(1)}(x)$, $\overline{g}^{(2)}(x)$, and $\overline{g}^{(3)}(x,y)$ has been calculated in several of these regimes and is shown in Figures 11.2
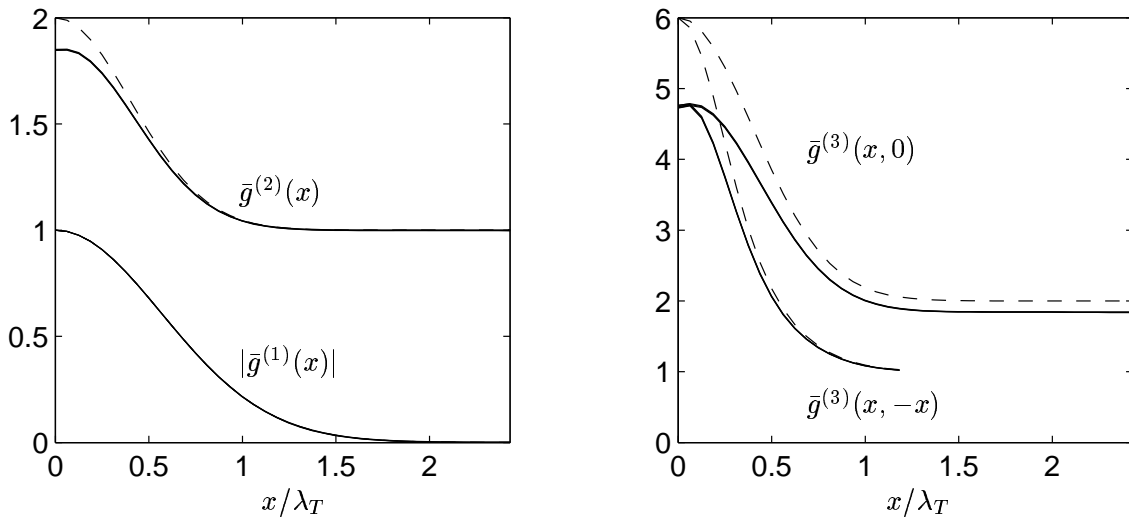
Figure 11.2: **Correlation functions in $\gamma = 5$, $\widetilde{T} = 1000$ decoherent classical gases.** Exact results are shown as SOLID lines, with triple lines indicating uncertainty (mostly not visible at this scale). DASHED lines show the ideal Bose gas values for comparison ($g^{(1)}(x)$ is indistinguishable). Here, $l_\rho = 10\pi\lambda_T$. $\mathcal{S} = 10^5$, $M = 80$, $L = 5\lambda_T$.

to 11.7. Exact results are also compared to ideal gas values. The simulated physical regimes were:

Classical decoherent regime ($\widetilde{T} \gg \mathbf{max}[1, \gamma^2]$)

This regime occurs while the thermal wavelength dominates the small scale behavior of the particles. In particular, while it is smaller than the interparticle spacing l_ρ and the effective scattering length a_{1D}. Correlation functions in a fairly strongly interacting part of this regime are shown in Figure 11.2. Correlations decay on the length scale of λ_T, with only a small reduction in close range correlation with respect to the ideal gas.

Quantum degenerate decoherent regime ($\sqrt{\gamma/2\pi^2} \ll \widetilde{T} \ll 1$)

Here the gas is degenerate, but phase coherence exists only on length scales l_ϕ shorter or of the same order as the healing length ξ^{heal}. This is not enough for any significant quasicondensate to form. Example correlations shown in Figure 11.3. The short-range correlations are still largely thermal $g^{(2)} > 1$, as for the classical gas, but a
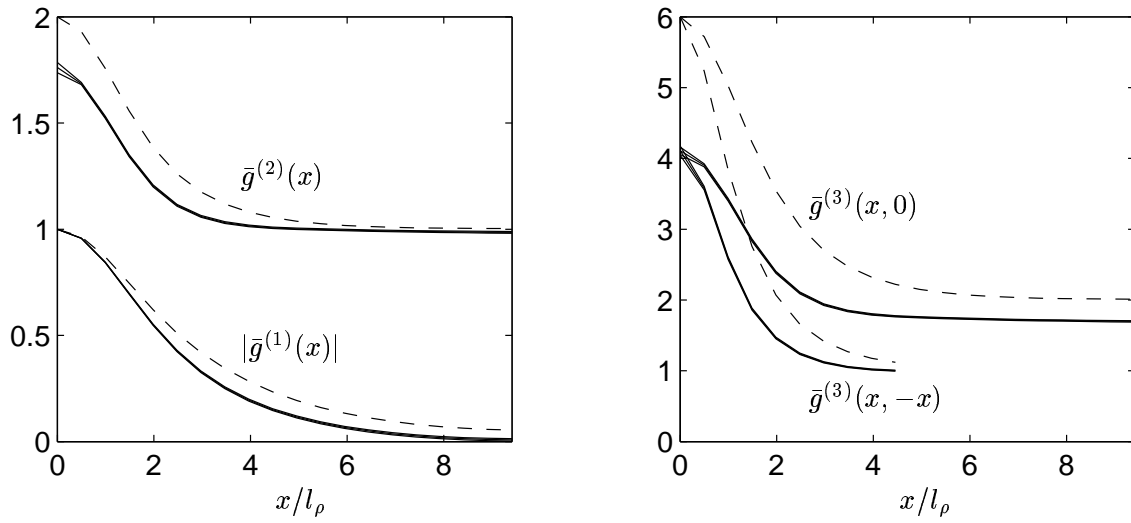
Figure 11.3: **Correlation functions in $\gamma = 0.03$, $\widetilde{T} = 0.236$ decoherent quantum degenerate gases.** Exact results are shown as SOLID lines, with triple lines indicating uncertainty (mostly not visible at this scale). DASHED lines show the ideal Bose gas values for comparison. Here, $\lambda_T = 2.06 l_\rho$. $\mathcal{S} = 10^5$, $M = 40$, $L = 5.14 l_\rho$.

systematic reduction of the range of all multi-particle correlations in comparison to the ideal gas is seen.

Fermionized nondegenerate regime ($1 \gg \widetilde{T} \ll \gamma^2$)

Here the fermion-like nature of strongly repulsive atoms dominates the small-scale behavior of the gas. The effective scattering length a_{1D} is much smaller than both the thermal wavelength and the interparticle spacing l_ρ leading to behavior similar to a hard-sphere (Tonks-Girardeau) model. In Figure 11.4, one sees strong antibunching on length scales a_{1D}, several times smaller than the phase coherence length. Three-particle correlations are also very strongly reduced at small distances $\lesssim a_{1D}$, with $|\overline{g}^{(3)}(0,0)| \lesssim 0.2$ in the example at $\gamma = 300$, $\widetilde{T} = 6000$ shown in Figure 11.4. This will lead to a strong reduction in three-particle inelastic scattering losses despite the very high temperature.
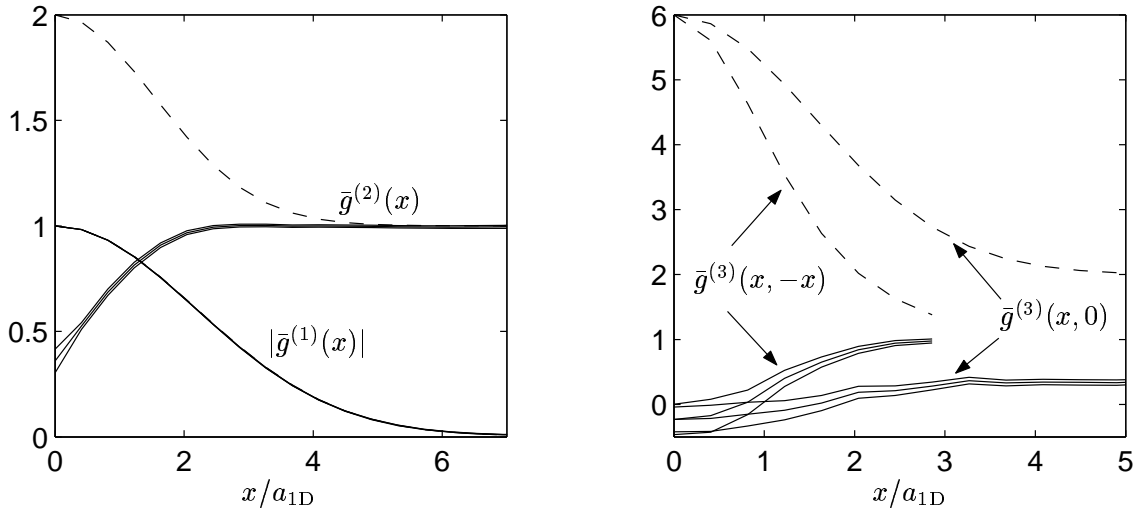
Figure 11.4: **Correlation functions in** $\gamma = 300$, $\widetilde{T} = 6000$ **strongly fermionized nonde-generate gases.** Exact results are shown as SOLID lines, with triple lines indicating uncertainty. DASHED lines show the ideal Bose gas values for comparison ($g^{(1)}(x)$ is indistinguishable). Here, $l_\rho = 300a_{1D}$, $\lambda_T = 3.873a_{1D}$, and $\xi^{\text{heal}} = 12.24a_{1D}$. $\mathcal{S} = 10^5$, $M = 36$, $L = 14.7a_{1D}$.

Transition regime with atom pairing ($\lambda_T \approx a_{1D} \approx \mathcal{O}(1)$)

Interesting new physical phenomena were seen in simulations of the transition regime where $\gamma \approx \widetilde{T} \approx \mathcal{O}(1)$. Here all the length scales of the system noted in Section 11.1.3 are of similar order, the exact relationship between them depending fairly sensitively on γ and $\widetilde{T}$. Because of the presence several competing processes, approximate methods do not usually give accurate quantitative predictions.

The transition between the nondegenerate fermionized gas and a decoherent quantum degenerate gas is shown in the sequence of Figures 11.4, 11.5, 11.6, and 11.3. Details of the three-particle correlations in the still-fermionized part of the transition are shown in Figure 11.7.

There is a parameter regime where a peak in correlations is seen at finite separations, indicating the appearance of **pairing between atoms**. The pairing arises at interparticle distances of

$$l_{\text{pair}} \approx \frac{\lambda_T}{2} \tag{11.33}$$

when λ_T and a_{1D} are of the same order. It appears to be a consequence of competition between repulsion, which promotes relative antibunching at short lengths, and
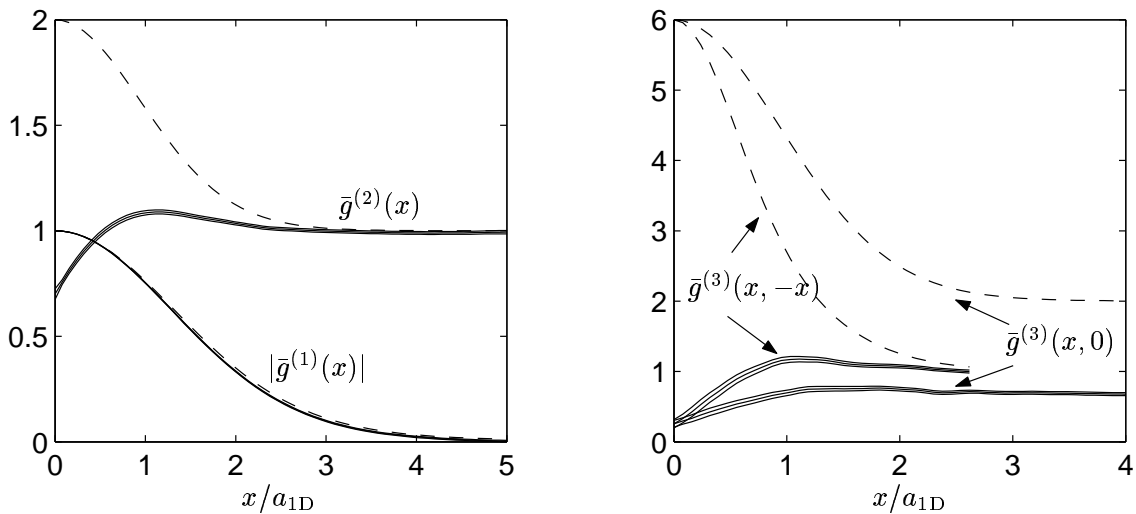
Figure 11.5: **Correlation functions in** $\gamma = 10$, $\widetilde{T} = 20$ **fermionized nondegenerate gases.**
Exact results are shown as SOLID lines, with triple lines indicating uncertainty. DASHED lines show
the ideal Bose gas values for comparison. Here, $l_\rho = 10a_{1D}$, $\lambda_T = \xi^{\text{heal}} = 2.24a_{1D}$. $\mathcal{S} = 10^5$,
$M = 135$, $L = 10.7a_{1D}$.

the inherent bunching in a thermal field on length scales $\lesssim \lambda_T$. Enhanced pairing
at distances l_{pair} is seen to occur both in situations where the point density corre-
lations $\overline{g}^{(0)}$ indicate local bunching (> 1 — e.g. Figure 11.6) or antibunching (< 1
— e.g. Figure 11.5). Enhanced three-particle correlations at distances $\approx l_{\text{pair}}$ were
also seen.

11.4.2 Momentum distributions

An example of a calculated momentum distribution in the transition region is shown
in Figure 11.8. At low momenta $k \lesssim k_T = \lambda_T/\sqrt{2\pi}$, the distribution is seen to be
intermediate between an the ideal gas Bose-Einstein distribution and the Fermi-
Dirac distribution for the same μ and T. One also sees that the density of states
function ρ_k from the exact Yang & Yang solution[87] differs significantly from the
actual distribution of momenta.

At intermediate momenta $k_T \lesssim k \lesssim 2k_T$, a depletion in comparison to the ideal
gas is seen, while very high momentum particles $k \gtrsim 2k_T$ are more common than
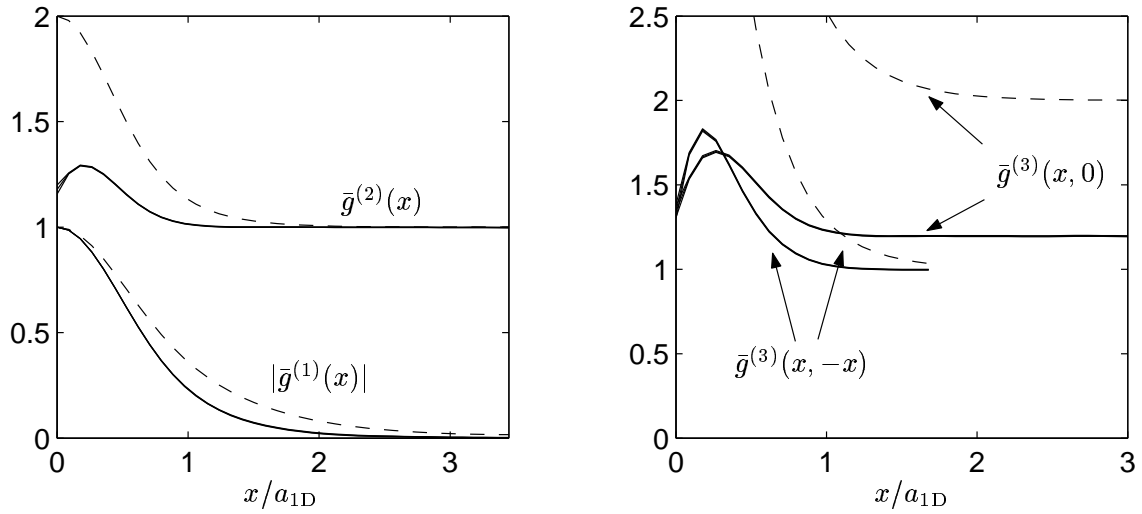in the ideal gas. This regime is shown in Figure 11.9, and one sees that the high

Figure 11.6: **Correlation functions in $\gamma = 1$, $\widetilde{T} = 1.6$ gases.** Exact results are shown as SOLID lines, with triple lines indicating uncertainty (mostly not visible at this scale). DASHED lines show the ideal Bose gas values for comparison. Here, $l_\rho = a_{1D}$, $\lambda_T = 0.793a_{1D}$, and $\xi^{\text{heal}} = 0.708a_{1D}$. $\mathcal{S} = 10^5$, $M = 80$, $L = 7.07a_{1D}$.
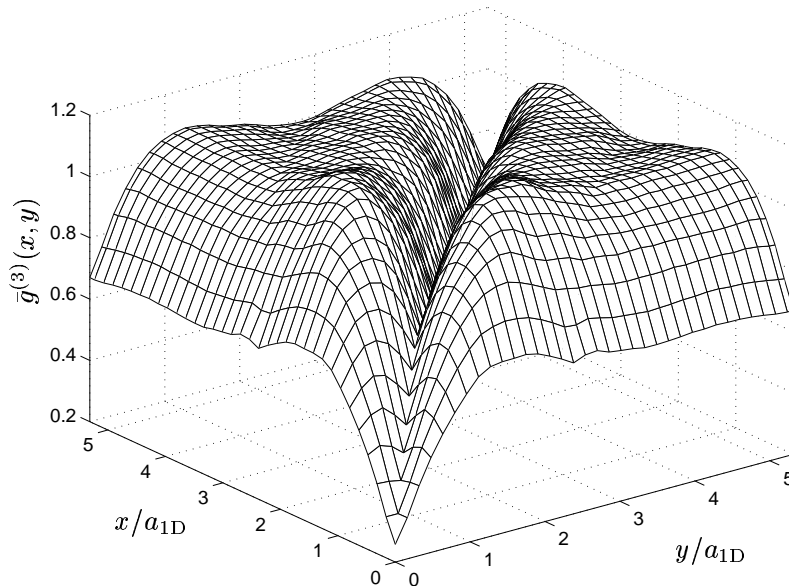

Figure 11.7: **General three-particle correlation function** in $\gamma = 10$, $\widetilde{T} = 20$ fermionized nondegenerate gases. Simulation details as in Figure 11.5.
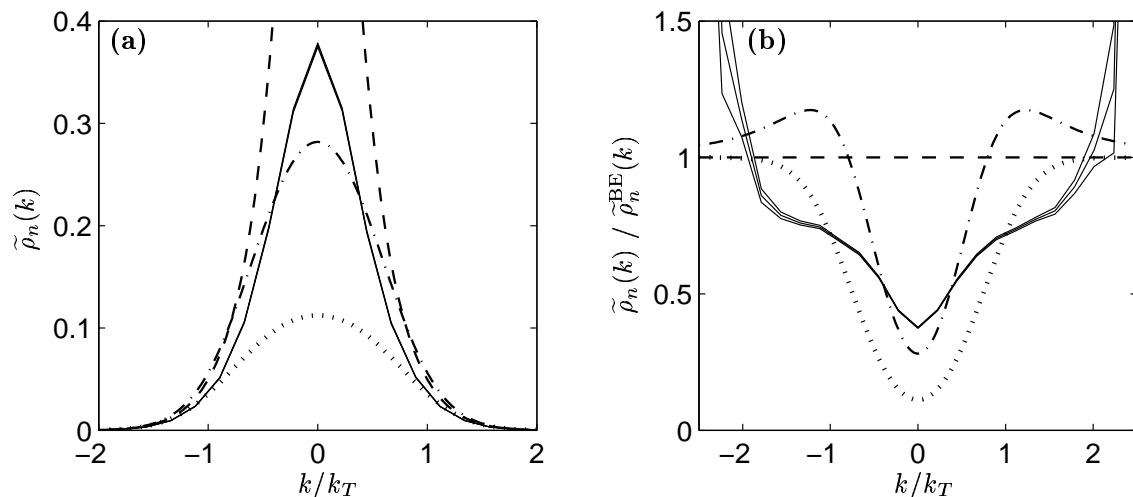
Figure 11.8: **Momentum distribution in the** $\gamma = 1$, $\widetilde{T} = 1.6$ **gases.** Solid lines indicate the results (with error bars) of a calculation with parameters as in Figure 11.6. Wave vectors k are scaled with respect to the thermal momentum $k_T = \lambda_T / \sqrt{2\pi}$, while the momentum distribution is normalized so that $\int \widetilde{\rho}_n(k) dk = 1$. Also shown for comparison are the Bose-Einstein ideal gas distribution (dashed), Fermi-Dirac distribution (dotted), and density of states ρ_k from the Yang & Yang exact solution[87] (dash-dotted), all calculated at the same T, μ, and g. These are normalized with the same factor as $\widetilde{\rho}_n$, rather than to unity. Subplot **(b)** shows the ratio with the ideal gas distribution $\widetilde{\rho}_n^{\mathrm{BE}}$ to resolve the high k behavior.

momentum distribution approaches the $T = 0$ power-law decay $\widetilde{\rho}(k) \propto k^{-4}$ found by Olshanii and Dunjko[97] from the exact Lieb and Liniger solution[86].

11.4.3   Comparison to exact Yang & Yang solution

As a test, these calculations have been compared with the density and energy per particle calculated from the Yang & Yang exact solution[87]. This is shown in Figure 11.10. At and around the importance sampling target time τ_T, the agreement is excellent. As expected, at $\tau \ll \tau_T$ the true distribution is badly sampled due to excessive spread in z_0. The indicator used to catch this problem is $\mathrm{var}\,[\mathrm{Re}\,\{z_0\}]$ (described in Section 10.1), which should be $\lesssim \mathcal{O}\,(10)$ to be confident of accuracy. For the case shown in Figure 11.10, this indicates accurate calculations at $\tau \geq 0.89\tau_T$, which is quite conservative. A similar comparison with $\overline{g}^{(2)}(0)$ values calculated[99] from the exact solution also shows agreement.
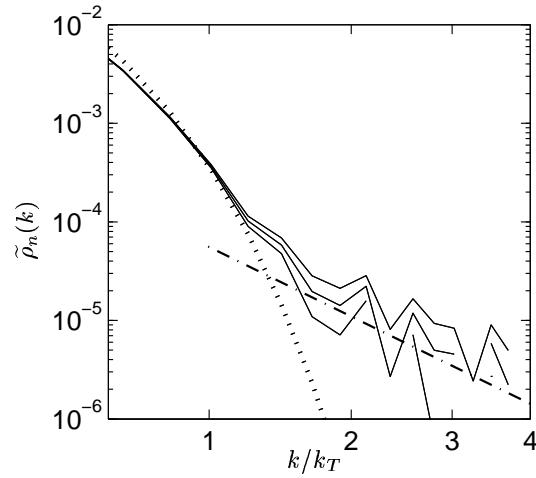
Figure 11.9: **Far tails of the momentum distribution in the $\gamma = 1$, $\widetilde{T} = 1.6$ gases.** Parameters as in Figure 11.8. SOLID triple lines indicate calculated normalized momentum distribution with error bars, DOTTED the Bose-Einstein ideal gas momentum distribution. The DOT-DASHED line shows the $T = 0$ high k asymptotic behavior[97].
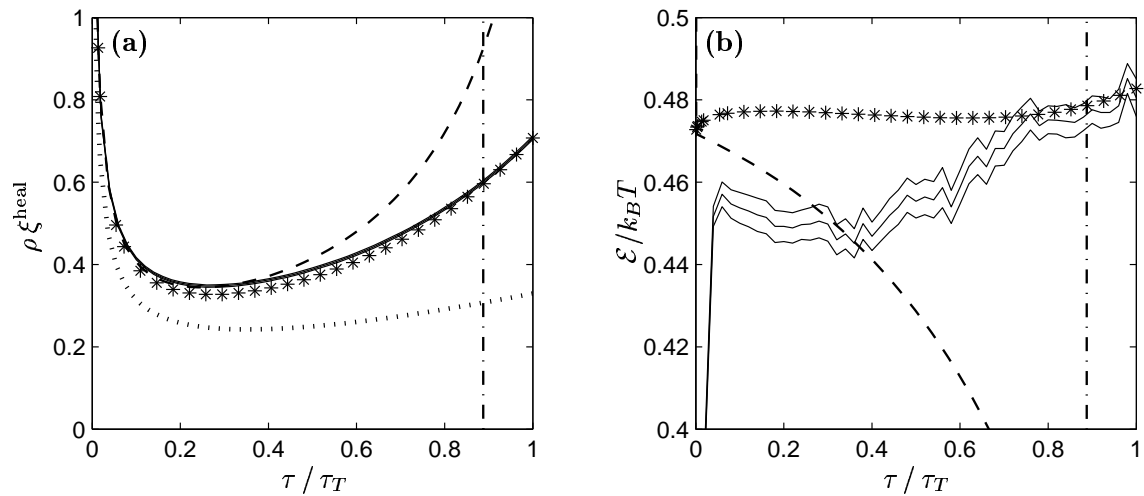

Figure 11.10: **Comparison of numerical calculation** (SOLID LINES with error bars) to exact solution (ASTERIXES) for the $\gamma = 1$, $\widetilde{T} = 1.6$ calculation with parameters given in Figure 11.6. **(a)**: density ρ, **(b)**: energy per particle $\mathcal{E}$. Ideal Bose gas (DASHED) and Fermi gas values also shown for comparison. The DASH-DOTTED vertical line indicates the lower limit on times τ for which accuracy is expected with a finite sample on the basis of the var $[\mathrm{Re}\,\{z_0\}] < 10$ indicator (See Appendix A).